Chemical Science

ROYAL SOCIETY OF CHEMISTRY

EDGE ARTICLE

View Article Online
View Journal | View Issue

Cite this: *Chem. Sci.*, 2025, **16**, 12104

All publication charges for this article have been paid for by the Royal Society of Chemistry

Received 28th February 2025
Accepted 27th May 2025

DOI: 10.1039/d5sc01599e

rsc.li/chemical-science

Precise construction of Pd superstructures with modulated defect properties for solar-driven organic transformation†

Henglei Jia, ‡*[a] Jingzhao Li,‡[ab] Fu-Kuo Chiang,‡[c] Hao Wang,[de] Fan Li,[a] Zhong-Qing Lin,[f] Qifeng Ruan *[de] and Chun-yang Zhang *[b]

Precisely controlling the spatial arrangement of nanostructures offers unique opportunities for tuning physical and chemical properties; however, it remains a great challenge due to the lack of effective synthetic methods. Herein, we present a wet-chemistry strategy for the synthesis of three-dimensional (3D) Pd superstructures (Pd SSs) by manipulating the growth kinetics. The strategy consists of two steps including (1) the formation of a tetrahedron-shaped Pd nanocrystal core and (2) the growth of four legs on each tip of the core. Interestingly, each leg can be built from one, two, or three arrowhead-like Pd nanocrystals. Moreover, Pd SSs exhibit unique defect-induced modulated structure properties due to the existence of periodic Pd vacancies, which can provide active sites for reactant molecule adsorption and activation. The Pd SSs exhibit excellent catalytic performance toward the oxidation of *o*-phenylenediamine (OPDA) under visible and near-infrared (NIR) light illumination. Both theoretical and experimental results demonstrate that the superior photocatalytic activity of Pd SSs is derived from the well-ordered 3D architecture, unique modulated defect properties, high-index facets, and large local electric field enhancement. This research sheds new light on the rational design and precise construction of 3D nanostructures, with potential applications in the fields of catalysis, nanotechnology, and biotechnology.

Introduction

Solar-driven organic molecule synthesis holds great promise in responding to energy and environmental challenges because it can convert solar energy into chemical energy in a green and sustainable way.[1–5] Among various organic transformations, the oxidation of *o*-phenylenediamine (OPDA) to 2,3-diaminophenazine (DAP) is highly significant because DAP can serve as a pivotal intermediate in manufacturing with broad utility in various fields (*e.g.*, production of conductive polymers, synthesis of carbon dots, detection of peroxides in analytical chemistry, and immunoassays).[6,7] Since OPDA is carcinogenic and toxic, the oxidation of OPDA may cause the degradation of organic pollutants. Traditionally, the oxidation of OPDA can be achieved with H_2O_2 as an oxidizing agent,[8,9] but the reaction rate is small and the selectivity is not very high. From the viewpoint of green chemistry, the harvesting of solar energy to drive the organic reaction under mild conditions will have more hopeful prospects. However, solar-driven oxidation of OPDA is seldom reported up to now. Palladium nanocrystals have witnessed an explosion of interest recently due to their excellent catalytic capability and well-controlled morphology.[10–17] Pd has been widely applied as the catalyst with high performance in organic synthesis (*e.g.*, Suzuki, Heck, and Stille coupling reactions).[18–22] In addition, Pd nanocrystals possess unique light-harvesting capability, with the photothermal conversion efficiency approaching 100%.[23–25] Therefore, Pd nanocrystals featuring excellent catalytic and optical properties are good candidates as photocatalysts for the oxidation of OPDA.

The catalytic performance of noble metal nanocrystals highly relies on their crystal facets and spatial architecture,[26–33] since the crystal facets and surface structure of noble metal nanocrystals, especially the atomic steps and kinks with low coordination sites that are vitally important to the catalytic process, are closely related to their spatial architecture. Consequently,

[a]*College of Chemistry, Chemical Engineering and Materials Science, Shandong Normal University, Jinan 250014, China. E-mail: hljia@sdnu.edu.cn*

[b]*School of Chemistry and Chemical Engineering, Southeast University, Nanjing 211189, China. E-mail: zhangcy@seu.edu.cn*

[c]*National Institute of Clean-and-Low-Carbon Energy, Beijing 102209, China*

[d]*Guangdong Provincial Key Laboratory of Semiconductor Optoelectronic Materials and Intelligent Photonic Systems, Harbin Institute of Technology, Shenzhen 518055, China. E-mail: ruanqifeng@hit.edu.cn*

[e]*Quantum Science Center of Guangdong-Hong Kong-Macao Greater Bay Area, Shenzhen-Hong Kong International Science and Technology Park, NO. 3 Binglang Road, Futian District, Shenzhen 518055, China*

[f]*Modern Experiment Technical Center, Anhui University, Hefei 230039, China*

† Electronic supplementary information (ESI) available. See DOI: https://doi.org/10.1039/d5sc01599e

‡ These authors contributed equally to this work.

the construction of Pd nanocrystals with a unique architecture is particularly attractive. Recently, considerable effects have been devoted to the morphology-controlled synthesis using wet-chemistry strategies, and Pd nanocrystals with different shapes have been achieved.[10–17] 3D well-organized superstructures composed of diverse building blocks are particularly notable with remarkable physicochemical properties and superior catalytic performance.[34–38] Nevertheless, the construction of Pd SSs has rarely been reported due to the lack of a wet-chemical approach. Moreover, the introduction of vacancy defects in Pd nanocrystals represents a promising strategy because these vacancies can provide active sites for molecule adsorption and activation and consequently promote the catalytic activity.[15,39–42] Therefore, the development of Pd SSs featuring modulated defect properties remains a challenge but is highly desired.

In this work, we present a facile synthetic strategy for the construction of 3D Pd SSs that consist of a tetrahedron-shaped Pd core and four legs grown on each tip of the Pd core by manipulating the kinetics of nanocrystal growth. The growth of Pd SSs consists of two stages, including (1) the formation of a tetrahedron-shaped Pd nanocrystal core and (2) the growth of four legs on each tip of the core, depending on the reduction rate of the precursor with different molecules as the surfactants. In addition, each leg of Pd SSs is built from the arrowhead-like Pd nanocrystals, and the number of nano-arrowheads can be simply controlled as one, two, and three. Moreover, the Pd SSs are rich in vacancy defects at the interface of two neighboring nano-arrowheads, which are formed during the growth process. Benefiting from the superstructure architecture, modulated defect properties, high-index facets, and large local electric field enhancement, the Pd SS-3 sample exhibits superior photocatalytic activity toward the oxidation of OPDA under visible and NIR light illumination, with a DAP yield that is 5.4 and 3.0 times that of Pd nano-tetrahedra and Pd nanosheets, respectively. We further systematically investigate the photocatalytic mechanism theoretically and experimentally.

Results and discussion

Synthesis and characterization of Pd SSs

Scheme 1 illustrates the growth process of Pd SSs through a kinetically controlled synthesis, which is achieved by tuning the reduction rate of the precursor palladium(II) acetylacetonate ($Pd(acac)_2$), using poly(vinylpyrrolidone) (PVP) and cetyltrimethylammonium bromide (CTAB) as surfactants and a mixture solution of *N*,*N*-dimethylpropanamide (DMP) and benzyl alcohol (BA) as the solvent. CO molecules are generally employed as the structure-directing agents for the anisotropic growth of Pd nanocrystals because they strongly adsorb onto the (111) planes.[10] Since the CO-involved synthetic strategies are relatively dangerous, CO release is achieved by the decomposition of $W(CO)_6$ and is subsequently used as both a structure-directing agent and a reducing agent in this work. Moreover, the limited release of CO from $W(CO)_6$ is beneficial for the formation of defect-rich Pd nanocrystals.[43] The whole growth process can be divided into two stages, the generation of a tetrahedron-shaped Pd core and the overgrowth of arrowhead-like Pd nanocrystals. The reduction rate of the precursor is of paramount importance for the growth process because $Pd(acac)_2$ can be reduced faster with PVP than CTAB as the surfactant. In the first stage, Pd nano-tetrahedra are first produced through the reduction of $Pd(acac)_2$ in the presence of PVP, which subsequently act as seeds for the next growth stage. In the second stage, the coordination of $Pd(acac)_2$ with CTAB would substantially slow down the reduction rate and induce a new growth mode to generate arrowhead-like Pd nanocrystals. Intriguingly, the number of nano-arrowheads can be readily controlled by changing the reaction conditions. The Pd SSs grown with one, two, and three nano-arrowheads are therefore named Pd SS-1, Pd SS-2, and Pd SSs-3 samples, respectively. Interestingly, the growth of the latter nano-arrowhead does not just occur on the former one, and there is a small angle between two adjacent nano-arrowheads. Notably, Pd vacancy defects arise extensively near the interface of two neighboring nano-arrowheads, which can function as active sites for molecular adsorption and activation.

Representative transmission electron microscopy (TEM) images of the Pd SS sample at a high and a low magnification are displayed in Fig. 1a and S1†. Each Pd SS consists of a dark core and three legs, since the fourth leg can hardly be observed in TEM mode. The number yield of the Pd SSs is 86.9%, and the average length of the legs is 44.9 ± 0.7 nm. High-angle annular dark-field scanning transmission electron microscopy (HAADF-STEM) images of a single Pd SS-3 taken in bright and dark field

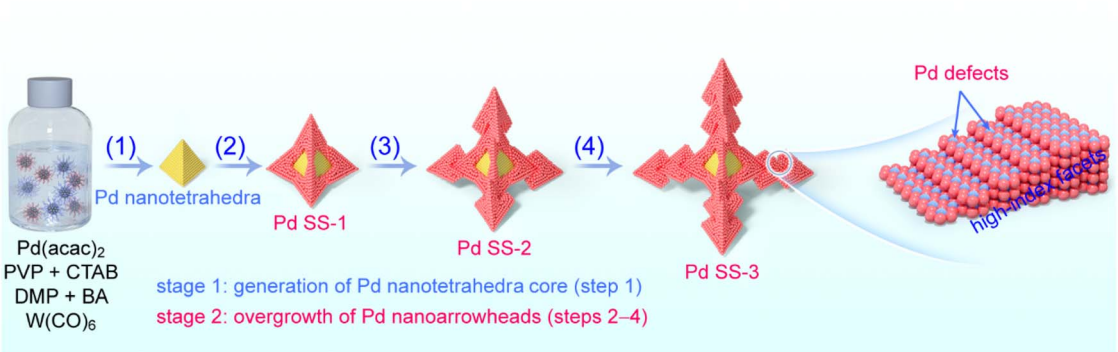

Scheme 1 Schematic illustration of the growth process of Pd SSs.

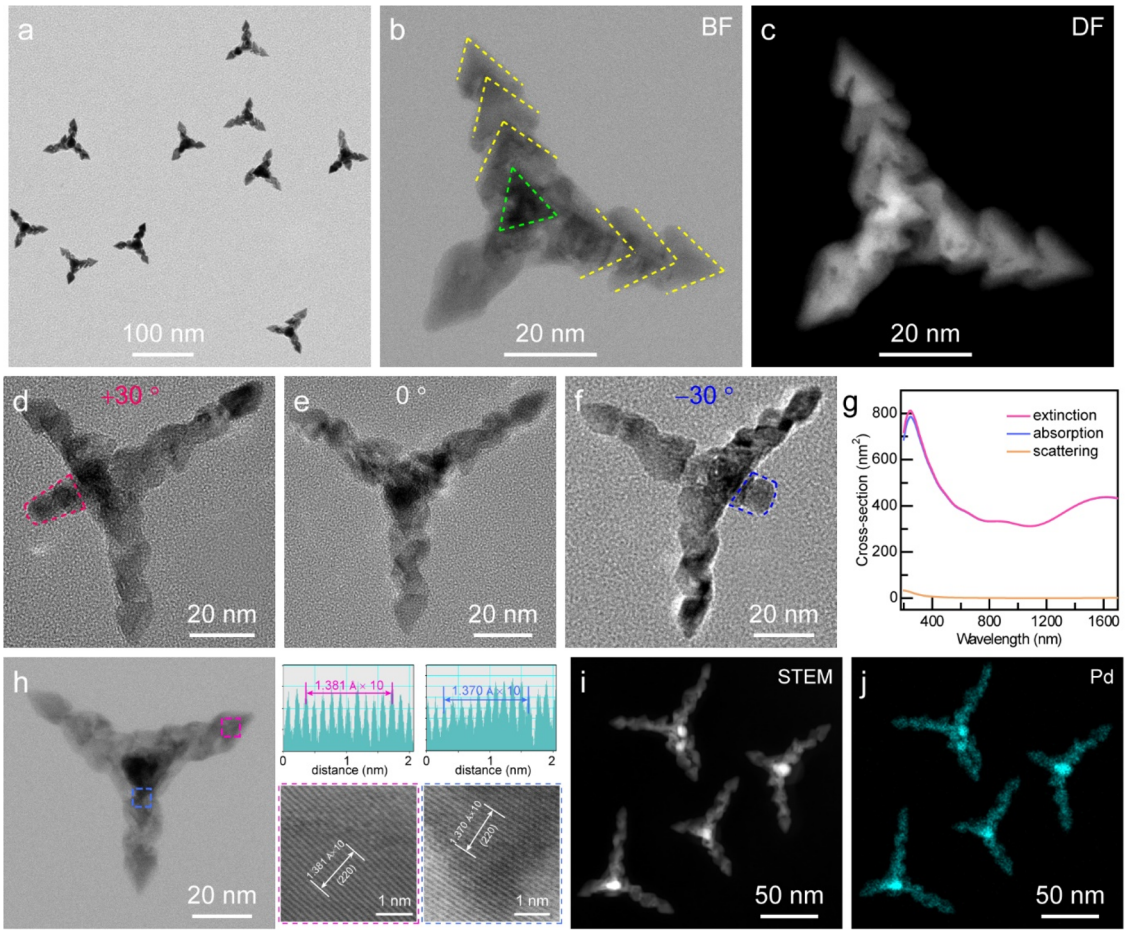

Fig. 1 Synthesis and characterization of Pd SSs. (a) Representative TEM image of the Pd SS sample. (b and c) HAADF-STEM images of a single Pd SS-3 sample taken in bright (b) and dark (c) field modes. (d–f) Tilting TEM studies. TEM images of the Pd SS sample after tilting it by +30° (d), 0° (e), and −30° (f). (g) FDTD simulated extinction (red), absorption (blue), and scattering (yellow) spectra of the Pd SS sample. (h) HRTEM image of a single Pd SS. (i and j) HAADF-STEM image (i) and the corresponding elemental map (j) of the Pd SS sample.

modes clearly confirm that the Pd SS is constructed with a tetrahedron-shaped Pd core and three legs comprising three arrowhead-like Pd nanocrystals (Fig. 1b and c). To gain more insight into the 3D architecture of Pd SSs, tilting TEM studies were performed. As displayed in Fig. 1d–f, only three legs appear without sample rotation; in contrast, the fourth leg can be clearly observed when the sample is tilted 30° to the right or left. After the sample rotation, the low-magnification TEM image and other representative single particle characterization results also confirm that almost all the Pd SSs possess four legs (Fig. S2†). Identical conclusions are obtained with a high-resolution scanning electron microscopic (SEM) imaging study (Fig. S3†). The above results substantiate that the Pd SS-3 sample consists of a tetrahedron-shaped Pd core and four legs built from three arrowhead-like Pd nanocrystals.

To reveal the optical properties of the Pd SSs, we tracked the spectral evolution during the growth process using extinction spectra (Fig. S4†). Prior to the introduction of $W(CO)_6$ to trigger the growth, the initial yellow reaction solution shows an absorption peak at 322 nm. Upon triggering the growth, the 322 nm peak vanishes, and meanwhile both a new peak at 272 nm and a broad absorption band spanning the visible to NIR regions emerge. When the reaction time increases, the intensity of the broad absorption peak initially increases and then declines slightly after 25 min, suggesting the formation of the Pd SS-3 sample. The excellent light-harvesting capability in the visible and NIR regions in combination with the inherent catalytic properties makes Pd SSs a promising material for solar-driven photocatalysts. Since the extinction peak can be contributed by light absorption and scattering,[44] to figure out the contribution of light absorption and scattering to the total extinction of Pd SSs, finite-difference time-domain (FDTD) simulations were performed by solving Maxwell's equations (Fig. 1g). The FDTD calculation results exhibit broad bands in the extinction spectrum, which result from the localized surface plasmon resonance (LSPR) properties of the intricate 3D Pd structures. Moreover, the calculated absorption-to-extinction fractions are both 0.999 for two broad bands (906 nm and 1568 nm), suggesting that Pd SSs are dominantly contributed to by light absorption. The LSPR properties and excellent light-harvesting capability over a broad spectral range offer good opportunity for the application of Pd SSs in solar energy conversion.

The crystalline properties of Pd SSs are identified from the X-ray diffraction (XRD) patterns, and the diffraction peaks can

only be indexed to Pd, indicating the highly crystalline nature of Pd SSs (Fig. S5†). This is supported by the aberration-corrected high-resolution transmission electron microscopy (HRTEM) imaging results (Fig. 1h). Energy-dispersive X-ray (EDX) elemental mapping results of four particles demonstrate the uniform dispersion of Pd element on three legs. The core is much brighter than the three legs due to the signal overlapping of the tetrahedron core with the fourth leg (Fig. 1i and j). The sample was further tilted 30°, and the EDX mapping results confirm that the fourth leg is also made of Pd (Fig. S6†).

The EDX spectra taken from the tetrahedron-shaped Pd core and one leg indicate that there are Pd, Cu, and C signals in the sample. Cu element originated from the Cu grid for TEM measurement and C was from the surfactant, further confirming that both the tetrahedron-shaped core and the legs are constructed of Pd. This is consistent with the observation from the X-ray photoelectron spectroscopy (XPS) survey spectrum (Fig. S7†). The high-resolution Pd 3d XPS spectrum can be deconvoluted into four peaks, two of which are attributed to the Pd^0 states (335.4 eV and 340.7 eV),[45] while the other two shoulders originate from the Pd^{2+} states (336.6 eV and 341.8 eV), with a Pd^0/Pd^{2+} ratio of 86 : 14 (Fig. S7b†). The appearance of Pd^{2+} state in the Pd SS sample results from the inevitable occurrence of surface oxidation or chemisorption of Pd(II) species.[46] Notably, the above XRD, XPS, and EDX analyses confirm the absence of detectable W signals in the sample, thereby excluding the incorporation of W into the Pd SSs.

Defect-induced modulated structure properties of Pd SSs

The precise manipulation of the electronic structure and surface properties of nanocrystals at the atomic level is a critical strategy for optimizing their catalytic performances. Defect

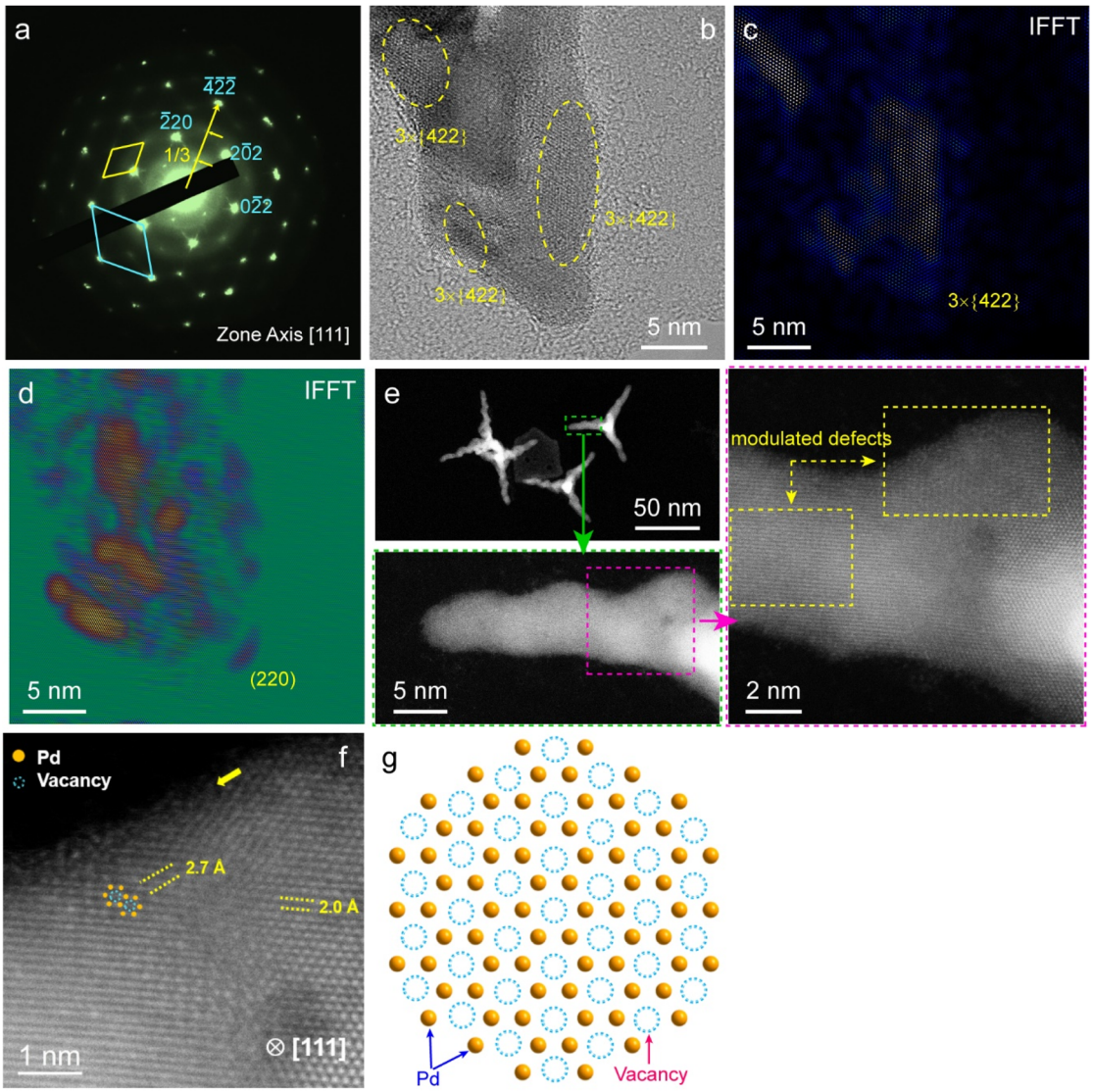

Fig. 2 Defect-induced modulated structure properties of the Pd SS sample. (a) SAED patterns of the Pd SS sample recorded along the [111] zone axis. (b–d) HRTEM (b) and the corresponding IFFT images (c and d) of the 3× {422} fringes. (e) HAADF-STEM images of the Pd modulated defects marked as dashed lines. (f) HRTEM images of the modulated defects observed in the [111] direction. The interplanar spacing of two modulated defects is 0.27 nm. (g) Schematic diagram of the Pd modulated structure.

engineering emerges as a promising methodology for tuning the electronic behaviors and catalytic activities of nanocrystals, which can effectively expose the active sites and modify the surface architecture.[47–49] Periodic defects can also induce modulated structures due to the long-period modulations superimposed on periodic substructures. Fig. 2a displays the selected area electron diffraction (SAED) patterns of the Pd SS sample acquired along the [111] zone axis. The SAED patterns confirm that Pd SSs are predominantly enclosed by {220} and {422} facets. Notably, the modulated 1/3 {422} reflection spots that correspond to 3 × {422} fringes can be clearly observed in the [111] electron diffraction pattern. The appearance of 1/3 {422} reflections generally originates from the defects in the face-centered cubic (fcc) metals.[26] HRTEM and inverse fast Fourier transform (IFFT) clearly revealed the presence of 3 × [422] lattice spacing of the fcc Pd crystal that is built of 3 sets of 3 × {422} spacing (Fig. 2b–d) because of the relationship between reciprocal space and real space. We therefore named these 3 × {422} fringes the defect-induced modulated structure. Careful observation of HAADF-STEM images shows that these modulated structures are mainly located at the interface of two nano-arrowheads (Fig. 2e). The interplanar space of these modulated structures was measured to be 0.27 nm, as displayed in Fig. 2f. Fig. 2g demonstrates the schematic diagram of the Pd modulated structures, which are constructed of six Pd atoms (orange circles) around one Pd vacancy (blue dotted circles). As discussed in previous studies, the presence of 1/3 {422} crystal planes is mainly caused by the stacking faults or twin planes because these diffraction spots are normally forbidden for a perfect fcc lattice.[26]

To investigate the atomic structure and coordination environment, X-ray absorption spectroscopy (XAS) of the Pd SS-3 sample was conducted (Fig. 3 and S8–S10†). Fig. 3a displays the Pd K-edge X-ray absorption near-edge structure (XANES) spectra of the Pd SS sample along with reference materials Pd foil and PdO. The edge features of Pd SSs are very close to those of Pd foil, which verifies that the valence state of Pd is mainly zero in Pd SSs. In addition, the absorption energy (E_0) of Pd in the Pd SSs is lower than that of PdO but is higher than that of Pd foil (inset in Fig. 3a), suggesting that Pd in the Pd SSs exhibits a more positive valence than metallic Pd, which may be due to surface oxidation. To gain a deep insight into the coordinate structure, the Pd K-edge extended X-ray absorption fine structure (EXAFS) spectra were acquired through Fourier transformation (Fig. 3b). The Pd SS sample exhibits a main peak at 2.50 Å, which is close to the Pd–Pd scattering of the first shell (2.55 Å) in Pd foil. Meanwhile, the Pd–O peak at 2.90 Å is absent similar to PdO, confirming the metallic state of Pd in the Pd SSs. To achieve a better understanding of the coordination environment of Pd in the Pd SSs, EXAFS curve fitting was conducted (Fig. S9 and S10†). The Pd–Pd coordination number from curving fittings for the Pd SS sample is 9.2, which is lower than that of 12 in Pd foil. The smaller Pd–Pd coordination number confirms that Pd atoms are coordinatively unsaturated. This is in accord with the HRTEM characterization results that the modulated structure phenomenon results from the presence of Pd vacancies in Pd SSs (Fig. 2f). Small wavelet transforms demonstrate that the intensity maximum of Pd SSs is similar to that of Pd foil, and the appearance of a very weak Pd–O peak is attributed to surface oxidation (Fig. 3c–e).

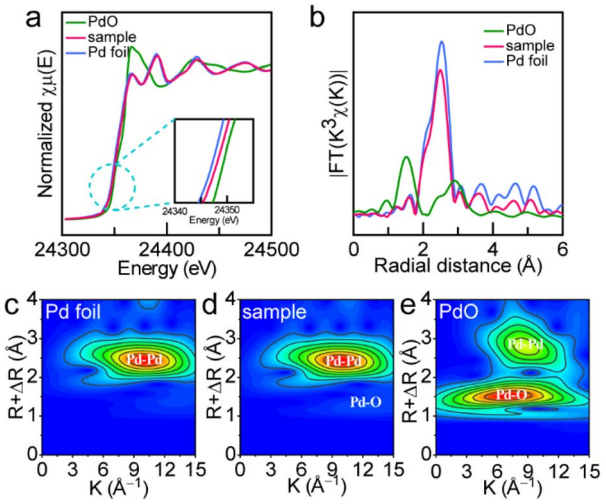

Fig. 3 Structural analysis of the Pd SS sample. (a and b) Normalized XANES spectra (a) and Fourier transforms of k^3-weighted Pd K-edge EXAFS spectra (b) of the Pd SS-3 sample in reference to Pd foil and PdO. (c–e) Small wavelet transforms of Pd K-edge EXAFS spectra of Pd foil (c), Pd SS-3 sample (d), and PdO (e).

Growth behaviour study of Pd SSs

To gain a better understanding of the growth behaviour of the Pd SSs, we performed a series of control experiments. First, the growth process was monitored to investigate the morphology evolution of the Pd SSs. The color of the starting reaction solution changed from yellow to brown after heating for 5 minutes (Fig. S11†). As shown in Fig. 4a, tetrahedron-shaped Pd nanocrystals are formed at this stage. When the color becomes dark brown at 7 minutes, one Pd nano-arrowhead grows on the Pd nanotetrahedron core (Fig. 4b). Subsequently, the color becomes darker and darker and two, three, and four Pd nano-arrowheads grow on the tetrahedron-shaped Pd core (Fig. 4c and d). The evolution results corroborate the fact that the growth process can be divided into two stages, the formation of a tetrahedron-shaped Pd core and the subsequent growth of Pd nano-arrowheads on the core. Second, we investigated the role of CTAB amount on the growth behaviour. In the absence of CTAB, only tetrahedron-shaped Pd nanocrystals can be obtained (Fig. 4e). When the CTAB amount is larger than 75 mg, Pd SSs begin to form (Fig. 4f–h). These control experiments verify that CTAB mainly functions as the surfactant in the second growth stage and is indispensable for the formation of nano-arrowheads. Third, we investigated the effect of PVP on the growth behaviour. No Pd nano-tetrahedra are formed without the addition of PVP molecules (Fig. 4i), implying that the first growth stage is contributed by the stability of the PVP surfactant. In addition, the molecular weight has a slight influence on the morphology of Pd SSs (Fig. S12†). Fourth, CO is generally employed as the structure-directing agent for the

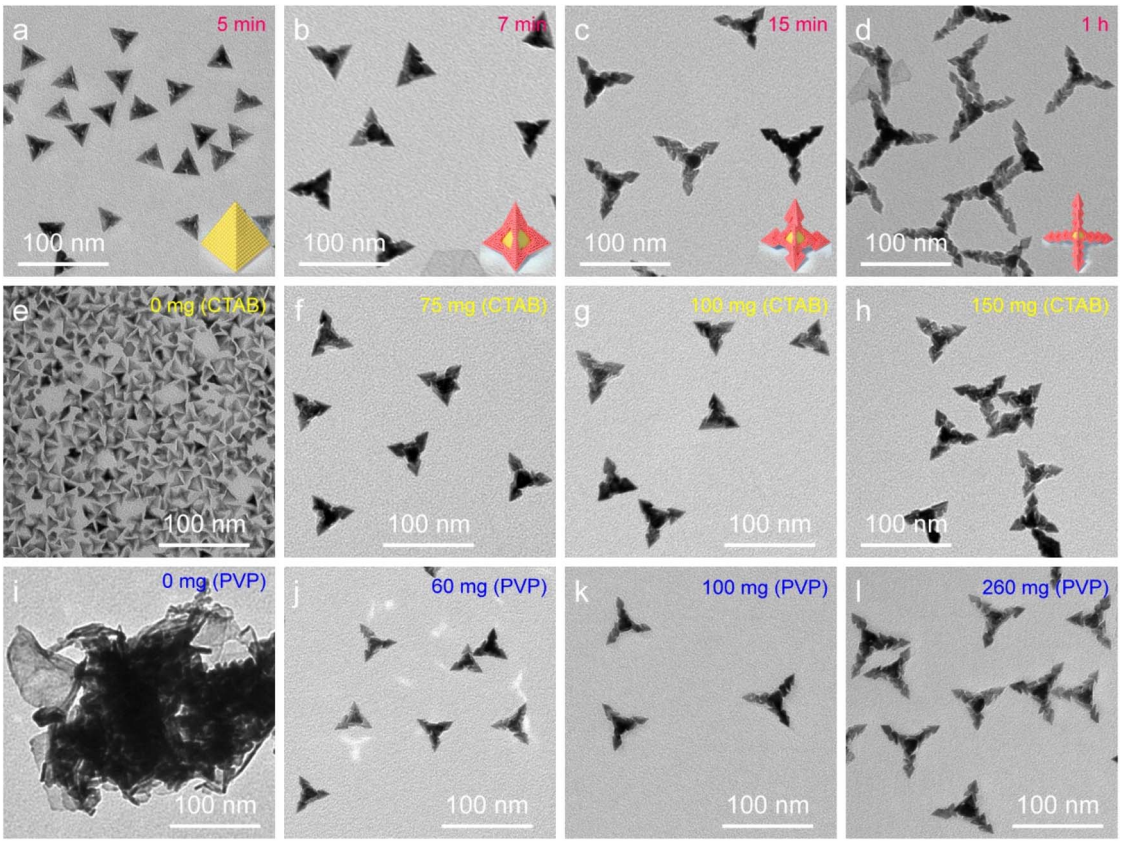

Fig. 4 Growth behaviour study. (a–d) TEM images of products at reaction times of 5 min (a), 7 min (b), 15 min (c) and 1 h (d), respectively. The insets show the spatial architectures of the products. (e–h) TEM images of products when the CTAB amounts are 0 mg (e), 75 mg (f), 100 mg (g) and 150 mg (h), respectively. (i–l) TEM images of products when the PVP amounts are 0 mg (i), 60 mg (j), 100 mg (k) and 260 mg (l), respectively.

growth of Pd nanocrystals in previous studies. In this work, CO release is achieved by the decomposition of $W(CO)_6$ (Fig. S13†). Without the addition of $W(CO)_6$, the reaction cannot be triggered (Fig. S13a†), implying that the reduction of $Pd(acac)_2$ precursor is relative to CO. When the amount of $W(CO)_6$ is insufficient, tetrahedron-shaped Pd nanocrystals, large Pd nanosheets, or Pd SS-1 was obtained (Fig. S13b and c†). These results suggest that CO participates in both stages as the reducing agent for the formation of Pd SSs. Fifth, the reducing capability of solvent that is composed of DMP and BA is also of great importance to the growth behavior (Fig. S14†) because the nucleation and growth of metal nanocrystals highly depend on their reduction rate.[26] In the absence of BA, only tetrahedron-shaped Pd nanocrystals are produced (Fig. S14a†). Since the reducing power of DMP is stronger than that of BA, a rapid reduction of precursor causes the formation of a large amount of nucleation centers and the subsequent growth of nano-arrowheads in the second stage is therefore inhibited. In contrast, excess BA would result in a very slow reduction rate and the generation of large Pd nanosheets, which change the growth behaviour (Fig. S14d†). The purity of BA used in this work is 99%, and the trace impurities in the reagents exert negligible influence on the synthesis outcomes. Therefore, an appropriate volume ratio of DMP to BA is crucial for the successful preparation of Pd SSs. Finally, the replacement of CTAB with cetyltrimethylammonium chloride (CTAC) has no influence on the morphology of Pd SSs (Fig. S15†), suggesting that the effect of halide ions on the morphology is not prominent in the growth process.

Solar-driven oxidation of OPDA

The well-organized spatial architecture, excellent light-harvesting capability, and unique modulated defect properties make Pd SSs a promising material as the catalyst for those applications in solar-driven chemical reactions. To evaluate the photocatalytic performance of Pd SSs, oxidation of OPDA to DAP under visible and NIR illumination was employed as the model reaction (Fig. 5a and S16†). The yield of product DAP was monitored using the absorption spectra because DAP exhibits an absorption peak at about 420 nm, and the concentration of DAP shows a linear relationship with its absorbance values (Fig. S17†). Five types of samples, including Pd nano-tetrahedra (Fig. S18†), Pd SS-1 (Fig. 4b), Pd SS-2 (Fig. 4c), Pd SS-3 (Fig. 1a), and Pd SS-4 (Fig. 4d), were employed as the catalysts for the photocatalysis. The weights of catalysts were adjusted to the same using inductively coupled plasma optical emission spectroscopy.

The photocatalytic performances of the catalysts highly rely on their spatial architectures. As displayed in Fig. 5b, the Pd SS-

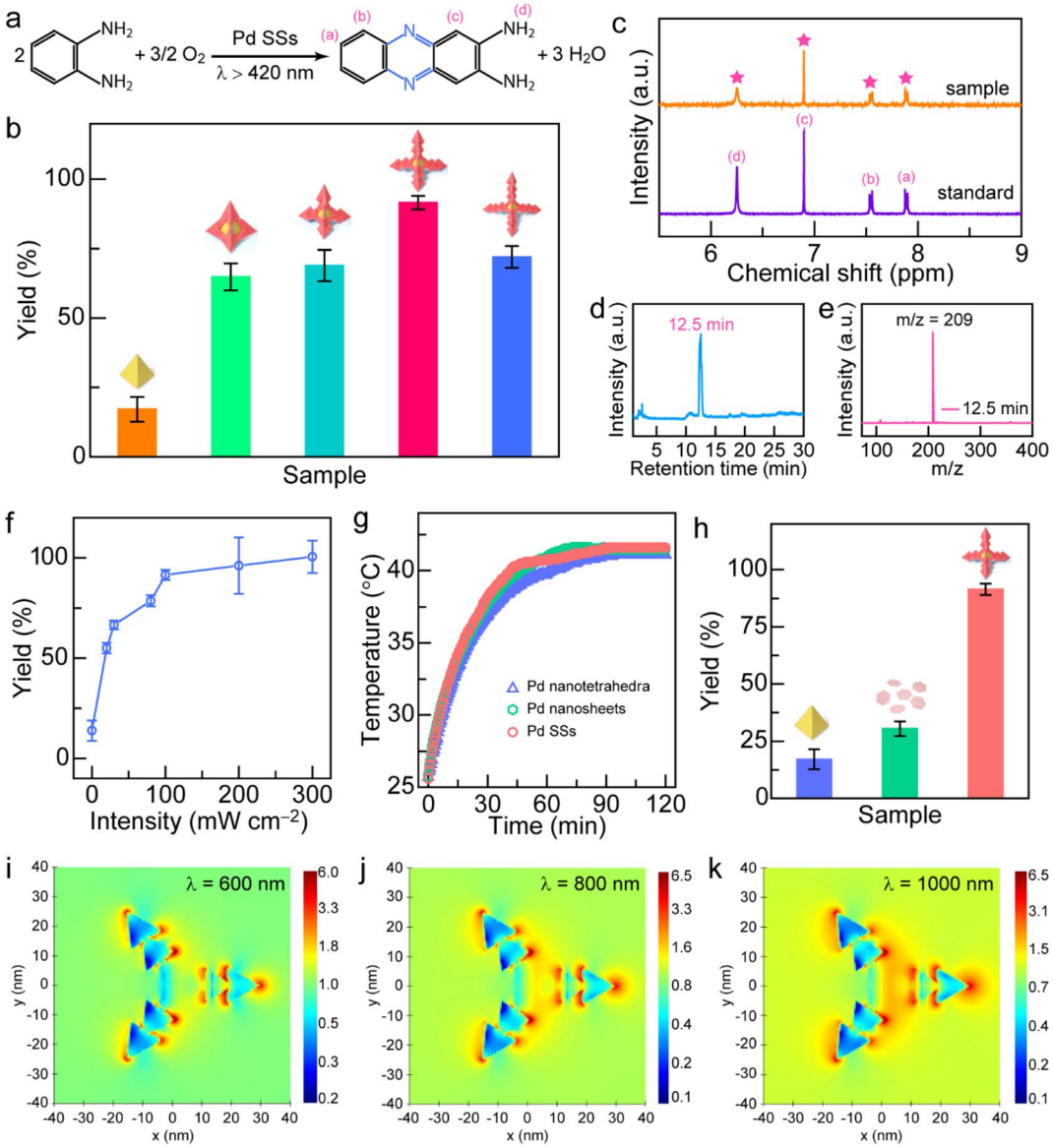

Fig. 5 Solar-driven oxidation of OPDA under visible and NIR light illumination. (a) Reaction equation. (b) Yields of DAP with Pd nano-tetrahedra, Pd SS-1, Pd SS-2, Pd SS-3, and Pd SS-4 samples as catalysts. (c) ^{1}H NMR spectra of the standard DAP solution (purple) and the reaction solution with the Pd SS-3 sample (yellow) as the catalyst. (d and e) LC-MS spectra of the reaction product. (f) Optical intensity-dependent photocatalytic activity. (g) Temperature rise traces of three different Pd nanocrystals under visible and NIR light illumination. (h) Comparison of photocatalytic activities with three different Pd nanocrystals as the catalysts. (i–k) FDTD-simulated electric field enhancement ($|E|/|E_0|$) contours drawn on the logarithmic scale under 600 nm (i), 800 nm (j), and 1000 nm (k) light excitation for the Pd SSs.

3 sample exhibits the best photocatalytic activity toward the oxidation of OPDA, followed by Pd SS-4, Pd SS-2, Pd SS-1, and Pd nano-tetrahedra. The yield of DAP with the Pd SS-3 sample as the catalyst is 91.5%, which is 5.4-fold that of Pd nano-tetrahedra. The photocatalytic activity of Pd nano-tetrahedra is significantly lower than those of the other four Pd SS samples, suggesting that the enhanced photocatalytic activity of Pd SSs predominantly results from the presence of arrowhead-like Pd nanocrystals within these nanostructures. In addition, the photocatalytic activities of Pd SS samples correlate with the number of arrowhead-like Pd nanocrystals. When the number increases, the photocatalytic activity gradually improves, suggesting that a higher proportion of arrowhead-like nanocrystals enhances the photocatalytic performance. The enhanced photocatalytic activity arises from the Pd vacancies on the arrowhead-like nanocrystals. The increase of Pd vacancies can provide more active sites for molecule adsorption and activation, thereby boosting the catalytic activity. However, when the number of arrowhead-like nanocrystals reaches four, the catalytic performance slightly decreases due to the relatively low yield of the Pd SS-4 sample. The commercial Pd/C is employed as the catalyst for comparison (Fig. S19†). The photocatalytic activity of the Pd SS-3 sample is 5.0-fold that of the Pd/C catalyst, further confirming that the photocatalytic

performance depends on the spatial architectures of the catalysts. Besides the spatial architectures, the optical properties of catalytic nanoparticles may affect their catalytic performances. The extinction spectra of these five types of catalysts reveal that the four Pd SS samples exhibit a broad absorption band spanning the visible to NIR regions (Fig. S4†), but the Pd nano-tetrahedra show weak absorption in the visible and NIR regions (Fig. S18c†), suggesting that the overlap between the optical absorption of the catalysts and the solar spectrum may influence the catalytic performance. The Pd SS-3 sample with excellent light-harvesting capability and a unique spatial architecture is therefore selected as the photocatalyst for the subsequent studies. The time-dependent absorption spectra of product DAP indicate that the oxidation of OPDA is driven by solar energy with Pd SSs as the catalyst (Fig. S20†). The yield of DAP increases significantly after the first 30 min of illumination, suggesting that this reaction can be triggered in about 30 min. When the reactant was consumed almost completely, the reaction rate was gradually decreased. The successful production of DAP was further cross-checked by ^{1}H nuclear magnetic resonance (NMR) and liquid chromatography–mass spectrometry (LC–MS). The chemical shifts at 7.9, 7.5, 6.9, and 6.3 ppm in the ^{1}H NMR spectrum arose from hydrogen atoms of DAP that are marked *a*, *b*, *c*, and *d* in Fig. 5a, respectively. The ^{1}H NMR peaks of the reaction solution after a typical photocatalytic process are consistent with those of the standard DAP solution (Fig. 5c), suggesting the successful production of DAP. In addition, the reaction solution has a strong absorption peak at a retention time of 12.5 min with an *m/z* value of 209, which is attributed to the product DAP (Fig. 5d and e). The OPDA peak of the reaction solution after the typical photocatalytic process can be hardly observed in the LC–MS spectrum, revealing the high activity of the catalyst. Both ^{1}H NMR and LC–MS results verify the high activity and selectivity of this reaction with Pd SSs as the catalyst.

To further reveal oxidation of OPDA is driven by solar energy, the dependence of photocatalytic activity on the optical intensity was investigated by performing the photocatalytic reaction under illumination with different light intensities (Fig. 5f and S21†). As shown in Fig. 5f, the photocatalytic activity increases rapidly when the light intensity is lower than 100 mW cm^{-2}, while the yield of DAP increases slowly when the light intensity becomes saturated, indicating that the oxidation of OPDA is indeed driven by light irradiation. Notably, the yield values reported here are acquired after 2.5 h of photocatalytic experiments conducted under different light intensities. When the light intensity exceeds 100 mW cm^{-2}, the product yield reaches 100% within this reaction period. However, at lower light intensities, the yields remain below 100% under identical conditions. Prolonging the reaction duration under these conditions ultimately results in the product yield of 100%. Control experiments confirm that the photocatalytic activity is low in the absence of light or catalyst (Fig. S22†), implying that the oxidation of OPDA is driven by light with Pd SSs as the catalyst. The reaction solution temperature is 41.5 °C under light irradiation. To investigate the contribution of photothermal effect on the photocatalytic activity, the oxidation of OPDA is performed in a 45 °C oil bath in the dark with the Pd SSs as the catalyst. The yield of DAP is 41.7%, implying that the photothermal effect has an influence on the photocatalytic activity. The photothermal effect has been extensively documented as a ubiquitous phenomenon in various metallic nanostructures, including Au, Ag, Al, Cu, Pt, and Pd.[19,50–54] The photothermal conversion efficiency depends on the type, size, and morphology of nanocrystals.[23] In comparison with other metal nanocrystals, Pd exhibits distinct advantages in photothermal catalysis due to their exceptional catalytic activities and remarkable thermal stabilities. In addition to the type of metal, the morphologies of Pd nanocrystals have a significant impact on the photothermal effect. The morphology-dependent photothermal conversion efficiencies of various differently shaped structures have been extensively investigated.[16,55–58] To further distinguish the contribution between the photothermal effect and photocatalysis, two other Pd nanocrystals, Pd nano-tetrahedra and Pd nanosheets were prepared and employed as catalysts (Fig. S18†). Fig. 5g demonstrates the temperature rise traces of the Pd SS, Pd nano-tetrahedron, and Pd nanosheet samples under light illumination, and all the traces show a similar trend. The temperature increases linearly and then reaches a plateau after about 100 min, with a final temperature of about 41.5 °C. The photothermal experiments indicate that these three Pd nanocrystals have similar photothermal capability; however, their photocatalytic performances are significantly different.

The photocatalytic activity of Pd SSs is about 5.4 and 3.0 times those of Pd nano-tetrahedra and Pd nanosheets, implying that the superior photocatalytic activity of the Pd SSs is not dominantly contributed to by the photothermal effect. In contrast, the unique spatial architecture and modulated defect properties of Pd SSs play a vital role in the oxidation of OPDA. To investigate the stability of Pd SSs in the photocatalytic experiment, we examined the STEM image, SAED pattern, and XPS spectrum of the Pd SS sample after a typical photocatalytic process (Fig. S23 and S24†). The STEM image clearly reveals that there is no morphological change in the tetrahedron-shaped Pd core and arrowhead-like Pd nanocrystals after the photocatalytic process (Fig. S23†). As revealed by the SAED patterns and XPS results, the modulated structure properties and chemical states remain unchanged, suggesting the excellent stability of the Pd SSs in the photocatalytic process.

As revealed by the above results, the photothermal effect has an influence on the photocatalytic activity but is not dominantly contributed. Since the catalytic process can be accelerated by metal nanocrystals through either photothermal effect or plasmonic photocatalysis, we next studied the effect of LSPR on the photocatalysis. As shown in Fig. 1g, FDTD calculations have confirmed that the broad extinction spectrum of Pd SSs arises from the LSPR properties of Pd SSs. Under plasmon resonance excitation, hot electrons and holes are generated in Pd SSs. These energetic charge carriers can take part in the catalytic reaction and facilitate the conversion of OPDA to DAP.[7] Given that the distribution of hot charge carriers depend on the electromagnetic field enhancement around the Pd nanocrystals, electromagnetic simulations were therefore conducted to shed

light on plasmonic photocatalysis. Fig. 5i–k demonstrate the electric field enhancement contours of the Pd SS-3 sample under different light excitation in the visible and NIR light regions. All three results verify that the electric field enhancement effect depends on the spatial architecture, and the large field enhancement is mainly located around the tips of the nano-arrowhead. Because the modulated defects are mainly located at the interface of two nano-arrowheads, these Pd vacancies can function as active sites for O_2 and OPDA molecule absorption and activation. The large field enhancement near the active sites boosts the generation of hot charge carriers and facilitates the conversion of OPDA to DAP. Based on the above finding, a rational reaction mechanism for photocatalytic oxidation of OPDA on Pd SSs is proposed (Fig. 6). On one hand, modulated structures are formed on the surface of arrowhead-shaped Pd nanocrystals during the growth process, which are associated with crystal defects. These modulated defects as well as high-index facets function as active sites for O_2 adsorption and activation, lowering the activation energy for the oxidation of OPDA. On the other hand, Pd SSs can harvest light and generate hot charge carriers under plasmon excitation. These energetic hot electrons and hot holes possess strong reduction and oxidation capability, accelerating the conversion from OPDA to DAP. Previous research has demonstrated that the photocatalytic process comprises two major stages including (1) the generation of $^{\bullet}OH$ radicals and (2) subsequent OPDA oxidation by these radicals (Fig. 6a).[7] The first stage plays a pivotal role in OPDA oxidation because the production of 1 mol of DAP requires the consumption of 6 mol of $^{\bullet}OH$ radicals. The formation of $^{\bullet}OH$ radicals occurs through two distinct pathways including (1) the reduction of adsorbed O_2 molecules by hot electrons, generating $^{\bullet}O_2^-$ intermediates that ultimately yield $^{\bullet}OH$ radicals, and (2) direct oxidation of OH^- species. The radicals primarily function to convert OPDA molecules into free radical intermediates, thereby lowering the reaction activation energy and promoting DAP formation. Moreover, the sharp tips of arrowhead-like Pd nanocrystals can induce large local electric field enhancement (Fig. 6b), facilitating both the generation of hot charge carriers and the synthesis of DAP. Benefiting from the large field enhancement, the modulated defect properties, and unique spatial architecture, the photocatalytic activity of the Pd SSs is boosted.

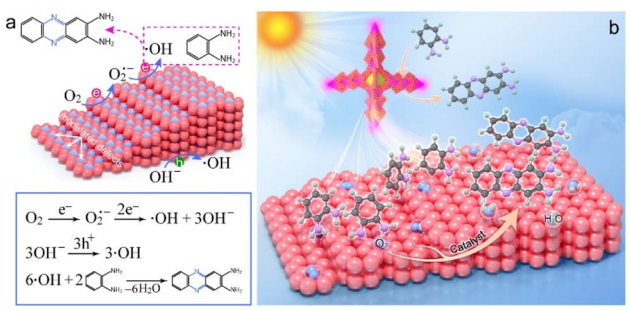

Fig. 6 Reaction mechanism of OPDA oxidation on Pd SSs under visible and NIR light illumination. (a) Reaction pathways. (b) Schematic illustration.

Conclusions

In summary, we have developed a controllable synthesis strategy for the construction of well-ordered Pd SSs. The obtained Pd SSs consist of a tetrahedron-shaped Pd core and four legs built from arrowhead-like Pd nanocrystals. The growth process can be divided into two stages by manipulating the growth kinetics, including (1) the generation of a tetrahedron-shaped Pd core and (2) the overgrowth of arrowhead-like Pd nanocrystals on the core. The obtained Pd SSs feature modulated structure properties due to the crystal defects formed during the growth process. Benefiting from the well-ordered spatial architecture, unique modulated defect properties, high-index facets, and large local electric field enhancement, the Pd SS-3 sample exhibits excellent catalytic activity toward the oxidation of OPDA to DAP under visible and NIR light illumination. The yield of DAP is about 5.4 and 3.0 times that of Pd nano-tetrahedron and Pd nanosheet samples, respectively. We propose a rational reaction mechanism based on experimental results and theoretical calculations. Given that Pd is a precious metal, future research should focus on exploring earth-abundant metals as the promising alternatives for photocatalyst discovery. This research provides a novel synthetic method for the construction of 3D well-organized architectures and sheds new light on the solar-driven chemical reaction in a green way.

Data availability

The data that support the findings of this study are available in the main article. Also, other relevant data for this study are available from the corresponding authors upon reasonable request.

Author contributions

H. L. Jia, J. Z. Li and F.-K. Chiang contributed equally to this work. H. L. Jia and C.-y. Zhang designed and supervised the project. J. Z. Li performed the experiments. F.-K. Chiang performed the HRTEM characterization and contributed to the study on modulated defect properties. H. Wang and Q. F. Ruan carried out the FDTD simulations and contributed to the data interpretation. F. Li assisted with the photocatalytic experiments and participated in discussions. Z.-Q. Lin performed the SEM characterization. H. L. Jia and C.-y. Zhang wrote the paper. All authors revised the manuscript and discussed the results.

Conflicts of interest

There are no conflicts to declare.

Acknowledgements

This work was supported by the National Natural Science Foundation of China (Grant No. 22375118), Guangdong Provincial Quantum Science Strategic Initiative (GDZX2306002), and Guangdong Pearl River Talent Program (2023QN10X058).

Notes and references

1 X. J. Lang, X. D. Chen and J. C. Zhao, *Chem. Soc. Rev.*, 2014, **43**, 473–486.
2 T. P. Yoon, M. A. Ischay and J. Du, *Nat. Chem.*, 2010, **2**, 527–532.
3 T.-C. Wang, B. K. Mai, Z. Zhang, Z. Y. Bo, J. D. Li, P. Liu and Y. Yang, *Nature*, 2024, **629**, 98–104.
4 D. Arena, E. Verde-Sesto, I. Rivilla and J. A. Pomposo, *J. Am. Chem. Soc.*, 2024, **146**, 14397–14403.
5 N. Zhang, X. Y. Li, H. C. Ye, S. M. Chen, H. X. Ju, D. B. Liu, Y. Lin, W. Ye, C. M. Wang, Q. Xu, J. F. Zhu, L. Song, J. Jiang and Y. J. Xiong, *J. Am. Chem. Soc.*, 2016, **138**, 8928–8935.
6 X.-G. Li, M.-R. Huang and W. Duan, *Chem. Rev.*, 2002, **102**, 2925–3030.
7 H. Zhang, S. H. Lam, Y. Z. Guo, J. H. Yang, Y. Lu, L. Shao, B. C. Yang, L. H. Xiao and J. F. Wang, *ACS Appl. Mater. Interfaces*, 2021, **13**, 51855–51866.
8 M. D. Xiao, C. M. Zhao, H. J. Chen, B. C. Yang and J. F. Wang, *Adv. Funct. Mater.*, 2012, **22**, 4526–4532.
9 J. H. Hu, H. Mi, N. Wang, H. Y. Zhu, W. Y. Guo, S. R. Zhang, F. Shi, Z. B. Lei, Z.-H. Liu and R. B. Jiang, *Nanoscale*, 2018, **10**, 5607–5616.
10 X. Q. Huang, S. H. Tang, X. L. Mu, Y. Dai, G. X. Chen, Z. Y. Zhou, F. X. Ruan, Z. L. Yang and N. F. Zhen, *Nat. Nanotechnol.*, 2011, **6**, 28–32.
11 H. Zhang, M. S. Jin, Y. J. Xiong, B. Lim and Y. N. Xia, *Acc. Chem. Res.*, 2013, **46**, 1783–1794.
12 Y. Dai, X. L. Mu, Y. M. Tan, K. Q. Lin, Z. L. Yang, N. F. Zheng and G. Fu, *J. Am. Chem. Soc.*, 2012, **134**, 7073–7080.
13 F. Wang, C. H. Li, L.-D. Sun, C.-H. Xu, J. F. Wang, J. C. Yu and C.-H. Yan, *Angew. Chem., Int. Ed.*, 2012, **51**, 4872–4876.
14 N. L. Yang, H. F. Cheng, X. Z. Liu, Q. B. Yun, Y. Chen, B. Li, B. Chen, Z. C. Zhang, X. P. Chen, Q. P. Lu, J. T. Huang, Y. Huang, Y. Zong, Y. H. Yang, L. Gu and H. Zhang, *Adv. Mater.*, 2018, **30**, 1803234.
15 H. J. Yu, T. Q. Zhou, Z. Q. Wang, Y. Xu, X. N. Li, L. Wang and H. J. Wang, *Angew. Chem., Int. Ed.*, 2021, **60**, 12027–12031.
16 S. S. Li, K. Gu, H. Wang, B. L. Xu, H. W. Li, X. H. Shi, Z. J. Huang and H. Y. Liu, *J. Am. Chem. Soc.*, 2020, **142**, 5649–5656.
17 Y. Zhang, X. Zhu, J. Guo and X. Q. Huang, *ACS Appl. Mater. Interfaces*, 2016, **8**, 20642–20649.
18 A. Balanta, C. Godard and C. Claver, *Chem. Soc. Rev.*, 2011, **40**, 4973–4985.
19 F. Wang, C. H. Li, H. J. Chen, R. B. Jiang, L.-D. Sun, Q. Li, J. F. Wang, J. C. Yu and C.-H. Yan, *J. Am. Chem. Soc.*, 2013, **135**, 5588–5601.
20 S. Handa, Y. Wang, F. Gallou and B. H. Lipshutz, *Science*, 2015, **349**, 1087–1091.
21 B. S. Takale, R. R. Thakore, G. Casotti, X. H. Li, F. Gallou and B. H. Lipshutz, *Angew. Chem., Int. Ed.*, 2021, **60**, 4158–4163.
22 Z. Y. Zhang, C. R. Rogers and E. A. Weiss, *J. Am. Chem. Soc.*, 2020, **142**, 495–501.
23 X. M. Cui, Q. F. Ruan, X. L. Zhuo, X. Y. Xia, J. T. Hu, R. F. Fu, Y. Li, J. F. Wang and H. X. Xu, *Chem. Rev.*, 2023, **123**, 6891–6952.
24 S. D. Marchi, S. Núñez-Sánchez, G. Bodelón, J. Pérez-Juste and I. Pastoriza-Santos, *Nanoscale*, 2020, **12**, 23424–23443.
25 Y. J. Zhang, R. Sha, L. Zhang, W. B. Zhang, P. P. Jin, W. G. Xu, J. X. Ding, J. Lin, J. Qian, G. Y. Yao, R. Zhang, F. C. Luo, J. Zeng, J. Cao and L.-P. Wen, *Nat. Commun.*, 2018, **9**, 4236.
26 Y. F. Shi, Z. H. Lyu, M. Zhao, R. H. Chen, Q. N. Nguyen and Y. N. Xia, *Chem. Rev.*, 2021, **121**, 649–735.
27 Z. X. Fan and H. Zhang, *Acc. Chem. Res.*, 2016, **49**, 2841–2850.
28 C. Chen, Y. J. Kang, Z. Y. Huo, Z. W. Zhu, W. Y. Huang, H. L. Xin, J. D. Snyder, D. G. Li, J. A. Herron, M. Mavrikakis, M. F. Chi, K. L. More, Y. D. Li, N. M. Markovic, G. A. Somorjai, P. D. Yang and V. R. Stamenkovic, *Science*, 2014, **343**, 1339–1343.
29 T.-H. Yang, J. Ahn, S. Shi, P. Wang, R. Q. Gao and D. Qin, *Chem. Rev.*, 2021, **121**, 796–833.
30 M. C. Luo, Z. L. Zhao, Y. L. Zhang, Y. J. Sun, Y. Xing, F. Lv, Y. Yang, X. Zhang, S. Hwang, Y. N. Qin, J.-Y. Ma, F. Lin, D. Su, G. Lu and S. J. Guo, *Nature*, 2019, **574**, 81–85.
31 M. Ha, J.-H. Kim, M. You, Q. Li, C. H. Fan and J.-M. Nam, *Chem. Rev.*, 2019, **119**, 12208–12278.
32 H. L. Jia, Y. Y. Yang, T. H. Chow, H. Zhang, X. Y. Liu, J. F. Wang and C.-y. Zhang, *Adv. Funct. Mater.*, 2021, **31**, 2101255.
33 H. L. Jia, F. Li, Y. Y. Yang, M. X. Zhao, J. Z. Li and C.-y. Zhang, *Chem. Sci.*, 2023, **14**, 5656–5664.
34 J. W. Lv, X. Q. Gao, B. Han, Y. F. Zhu, K. Hou and Z. Y. Tang, *Nat. Rev. Chem.*, 2022, **6**, 125–145.
35 J. Guo, Y. Zhang, L. Shi, Y. F. Zhu, M. F. Mideksa, K. Hou, W. S. Zhao, D. W. Wang, M. T. Zhao, X. F. Zhang, J. W. Lv, J. Q. Zhang, X. L. Wang and Z. Y. Tang, *J. Am. Chem. Soc.*, 2017, **139**, 17964–17972.
36 Y. Y. Yang, H. L. Jia, N. N. Hu, M. X. Zhao, J. Z. Li, W. H. Ni and C.-y. Zhang, *J. Am. Chem. Soc.*, 2024, **146**, 7734–7742.
37 Y. C. Pi, N. Zhang, S. J. Guo, J. Guo and X. Q. Huang, *Nano Lett.*, 2016, **16**, 4424–4430.
38 Q. S. Wang, H. Wang, Y. Yang, L. H. Jin, Y. Liu, Y. Wang, X. Y. Yan, J. Xu, R. Q. Gao, P. P. Lei, J. J. Zhu, Y. H. Wang, S. Y. Song and H. J. Zhang, *Adv. Mater.*, 2019, **31**, 1904836.
39 Y. P. Zhao, Z. F. Chen, N. N. Ma, W. Y. Cheng, D. Zhang, K. C. Cao, F. Feng, D. D. Gao, R. J. Liu, S. J. Li and C. Streb, *Adv. Sci.*, 2024, **11**, 2405187.
40 X. T. Zhang, L. Hui, D. X. Yan, J. Z. Li, X. Chen, H. Wu and Y. L. Li, *Angew. Chem., Int. Ed.*, 2023, **62**, e202308968.
41 Y. Zhang, S. B. Han, S. Q. Zhu, R. H. Chen, T. H. Li, Z. H. Lyu, M. Zhao, M. Gu, M. H. Shao and Y. N. Xia, *Angew. Chem., Int. Ed.*, 2023, **62**, e202314634.
42 Y. Zhang, B. L. Huang, Q. Shao, Y. G. Feng, L. K. Xiong, Y. Peng and X. Q. Huang, *Nano Lett.*, 2019, **19**, 6894–6903.
43 S. Dutta, B. S. Gu and I. S. Lee, *Angew. Chem., Int. Ed.*, 2023, **62**, e202312656.
44 W. H. Ni, X. S. Kou, Z. Yang and J. F. Wang, *ACS Nano*, 2008, **2**, 677–686.

45 Y. Y. Yang, H. L. Jia, S. H. Su, Y. D. Zhang, M. X. Zhao, J. Z. Li, Q. F. Ruan and C.-y. Zhang, *Chem. Sci.*, 2023, **14**, 10953–10961.
46 H.-C. Peng, S. F. Xie, J. Park, X. H. Xia and Y. N. Xia, *J. Am. Chem. Soc.*, 2013, **135**, 3780–3783.
47 A. Janssen, O. N. Nguyen and Y. N. Xia, *Angew. Chem., Int. Ed.*, 2021, **60**, 12192–12203.
48 F. Ikram, S. Cheong, I. Persson, Z. R. Ramadhan, A. R. Poerwoprajitno, J. J. Gooding and R. D. Tilley, *J. Am. Chem. Soc.*, 2025, **147**, 10784–10790.
49 M. Nasilowski, B. Mahler, E. Lhuillier, S. Ithurria and B. Dubertret, *Chem. Rev.*, 2016, **116**, 10934–10982.
50 J. X. Chen, J. Feng, Z. W. Li, P. P. Xu, X. J. Wang, W. W. Yin, M. Z. Wang, X. W. Ge and Y. D. Yin, *Nano Lett.*, 2019, **19**, 400–407.
51 D. Renard, S. Tian, M. H. Lou, O. Neumann, J. Yang, A. Bayles, D. Solti, P. Nordlander and N. J. Halas, *Nano Lett.*, 2021, **21**, 536–542.
52 Y. Xin, K. F. Yu, L. T. Zhang, Y. R. Yang, H. B. Yuan, H. L. Li, L. B. Wang and J. Zeng, *Adv. Mater.*, 2021, **33**, 2008145.
53 X.-M. Zhu, H.-Y. Wan, H. L. Jia, L. Liu and J. F. Wang, *Adv. Healthcare Mater.*, 2016, **5**, 3165–3172.
54 P. H. Zhao, Z. K. Jin, Q. Chen, T. Yang, D. Y. Chen, J. Meng, X. F. Lu, Z. Gu and Q. J. He, *Nat. Commun.*, 2018, **9**, 4241.
55 S. D. Marchi, S. Núñez-Sánchez, G. Bodelón, J. Pérze-Juste and I. Pastoriza-Santos, *Nanoscale*, 2020, **12**, 23424–23443.
56 J.-W. Xiao, S.-X. Fan, F. Wang, L.-D. Sun, X.-Y. Zheng and C.-H. Yan, *Nanoscale*, 2014, **6**, 4345–4351.
57 S. H. Tang, M. Chen and N. F. Zheng, *Small*, 2014, **10**, 3139–3144.
58 X. Q. Huang, S. H. Tang, J. Yang, Y. M. Tan and N. F. Zheng, *J. Am. Chem. Soc.*, 2011, **133**, 15946–15949.